



# Statistical Study on the Solar Wind Turbulence Spectra Upstream of Mars

Zhuxuan Zou<sup>1,2</sup> , Yuming Wang<sup>1,2</sup> , Zhenpeng Su<sup>1,2</sup> , Long Cheng<sup>1,2</sup> , Zhiyong Wu<sup>1,2</sup> , Tielong Zhang<sup>2,3,4</sup> ,  
Guoqiang Wang<sup>4</sup> , Sudong Xiao<sup>4</sup>, Yutian Chi<sup>5</sup> , Zonghao Pan<sup>1,2</sup> , Xinjun Hao<sup>1,2</sup> , Yiren Li<sup>1,2</sup> , and Kai Liu<sup>1,2</sup>

<sup>1</sup> National Key Laboratory of Deep Space Exploration/School of Earth and Space Sciences, University of Science and Technology of China, Hefei 230026, People's Republic of China; [ymwang@ustc.edu.cn](mailto:ymwang@ustc.edu.cn)

<sup>2</sup> CAS Center for Excellence in Comparative Planetology/CAS Key Laboratory of Geospace Environment/Mengcheng National Geophysical Observatory, University of Science and Technology of China, Hefei 230026, People's Republic of China

<sup>3</sup> Space Research Institute, Austrian Academy of Sciences, Graz, Austria

<sup>4</sup> Institute of Space Science and Applied Technology, Harbin Institute of Technology, Shenzhen, 518055, People's Republic of China

<sup>5</sup> Institute of Deep Space Sciences, Deep Space Exploration Laboratory, Hefei 230026, People's Republic of China

Received 2024 December 27; revised 2025 May 19; accepted 2025 June 8; published 2025 July 15

## Abstract

We statistically analyze the power spectral density (PSD) of magnetic field turbulence in the upstream solar wind of the Martian bow shock by investigating the data from Tianwen-1 and Mars Atmosphere and Volatile Evolution (MAVEN) during 2021 November 13 and December 31. The spectral indices and break frequencies of these PSDs are automatically identified. According to the profiles of the PSDs, we find that they could be classified into three types: A, B, and C. Only less than a quarter of the events exhibit characteristics similar to the 1 au PSDs (Type A). We observe the energy injection in more than one-third of the events (Type B), and the injected energy usually results in the steeper spectral indices of the dissipation ranges. We find the absence of the dissipation range in over one third of the PSDs (Type C), which is likely due to the dissipation occurring at higher frequencies rather than proton cyclotron resonant frequencies. We also find that the two spacecraft observed different types of PSDs in more than half of the investigated episodes, indicating significant variability upstream of the Martian bow shock. For example, the Type-B PSDs are more often seen by Tianwen-1, which was near the flank of the bow shock, than by MAVEN near the nose. This statistical study demonstrates the complicated turbulent environment of the solar wind upstream of the Martian bow shock.

*Unified Astronomy Thesaurus concepts:* [Interplanetary turbulence \(830\)](#); [Interplanetary physics \(827\)](#); [Pickup ions \(1239\)](#); [Mars \(1007\)](#); [Magnetic fields \(994\)](#); [Solar wind \(1534\)](#)

## 1. Introduction

Turbulence is ubiquitous in the space plasma's environment, in which the magnetic energy is injected at very large scales, cascades down to small scales, and dissipates in the kinetic range. These processes define the energy-containing range, inertial range, and dissipation range (G. Zimbardo et al. 2010; V. Carbone 2012; O. Alexandrova et al. 2013).

The energy transfer process is reflected in the power-law spectrum of the magnetic fluctuations, which has been observed extensively at 1 au. The energy-containing range, whose spectral index is typically  $\sim -1$  (W. H. Matthaeus & M. L. Goldstein 1986), is mainly below  $\sim 0.001$  Hz in 1 au and lower at the Martian orbit (N. Davis et al. 2023; M. Dorseth et al. 2024). The spectral index of the inertial range is always near the Kolmogorov scaling of  $-5/3$  (J. J. Podesta et al. 2007; J. E. Borovsky 2012). The break points at the high frequency of the inertial range are near the ion kinetic scales, such as the ion gyrofrequency or the ion plasma frequency, which are associated with Alfvén wave dispersion, damping, and current sheets (O. Alexandrova et al. 2008; S. A. Markovskii et al. 2008; C. W. Smith et al. 2012; Y. Narita 2016; L. D. Woodham et al. 2018). The typical spectral index of the dissipation range is  $\sim -8/3$  (O. Alexandrova et al. 2008, 2012). In the electron scales, the spectra become steeper and may not be power-law spectra (O. Alexandrova et al. 2009). In some

observations, the transition region could appear between the inertial range and the dissipation range, which is steeper than the dissipation range (K. H. Kiyani et al. 2015; S. Y. Huang et al. 2021).

Some spacecraft, such as the Parker Solar Probe (PSP; G. Jannet et al. 2021), Ulysses (A. Balogh et al. 1992), and MESSENGER (B. J. Anderson et al. 2007), help us to observe the turbulence at different heliocentric distances (R. Bruno & L. Trenchi 2014; R. Bruno et al. 2014; D. Duan et al. 2020). With the heliocentric distance decreasing from 0.7 to 0.1 au, the spectral indices of the inertial range increases from  $-5/3$  to  $-3/2$ , and the spectral indices of the dissipation range decreases from  $-3$  to  $-4$ , which is probably related to the cross-helicity and residual energy (C. H. K. Chen et al. 2020; S. Lotz et al. 2023). The break-point frequencies between the inertial range and dissipation range increase with decreasing heliocentric distance in the fast solar wind seemingly (R. Bruno & L. Trenchi 2014). In the slow solar wind, the same law is observed, but normalized by the ion cyclotron resonant frequency, the break-point frequencies have no relationship with the heliocentric distance (D. Duan et al. 2020), causing the dependence of the break-point frequency on the heliocentric distance in the fast solar wind to be questionable.

Mars has an ionosphere and small residual crustal magnetic fields, resulting in a small induced magnetosphere. The exosphere of Mars can exceed the bow shock and therefore the solar wind can directly interact with neutral atoms, resulting in an upstream solar wind environment distinct from Earth's and interplanetary space (C. Mazelle et al. 2004;

M. Delva et al. 2011). S. Ruhunusiri et al. (2017) divided the spectra into the MHD range (i.e., inertial range) and the Kinetic range (i.e., dissipation range) according to the local proton gyrofrequency and calculated the spectral indices in different regions and under different upstream solar wind conditions. However, the local proton gyrofrequency may not demarcate inertial and dissipation ranges, and therefore the distribution of the spectral indices may not be accurate. Therefore, in this paper, we statistically study the spectra of the solar wind turbulence upstream of Mars using a more careful method.

In the next section, we introduce the data used in our work and the method to obtain the spectral indices and break frequencies. In Section 3, we introduce our classifications of Martian turbulence spectra in the solar wind. In Sections 4 and 5, the characteristics of spectral indices and break frequencies are exhibited respectively. Section 6 introduces the spatial features of Martian turbulence spectra. Section 7 briefly summarizes the main results of this paper.

## 2. Data and Method

### 2.1. Data

China's first Mars mission, Tianwen-1, has been detecting the Martian space magnetic field since 2021 November 13 (Y. Wang et al. 2023; Z. Zou et al. 2023). Its magnetometer (MOMAG) operates at a sampling frequency of 32 Hz when the orbiter is both near the periareion and the apoareion in time spans of 120 minutes and 60 minutes, respectively, and at a sampling frequency of 1 Hz during other periods (K. Liu et al. 2020; Y. Wang et al. 2023). The Mars Atmosphere and Volatile Evolution (MAVEN) spacecraft's magnetometer (MAG) measures vector magnetic fields at 32 Hz since 2014 (J. E. P. Connerney et al. 2015). The Solar Wind Ion Analyzer (SWIA) in MAVEN provides plasma data (J. S. Halekas et al. 2015). To investigate upstream Martian solar wind turbulence, the paper uses the 32 Hz magnetic field data during 2021 November 13–December 31.

Upstream bow shock magnetic field data sets were manually selected based on bow shock crossing signatures (Y. Wang et al. 2023). Tianwen-1 and MAVEN had different orbital periods and were located in different regions during the period of interest. Tianwen-1 was positioned near the bow shock flank, while MAVEN remained near the nose when they were in the solar wind as shown in Figure 1. The sampling interval's limit of MOMAG mentioned before results in the Tianwen-1 data sets being localized in two distant areas. Thus, the total time of Tianwen-1 in solar wind is different from that of MAVEN. We use a 13 minute step size with a shifting step of 6.5 minutes to generate the spectra of the magnetic field fluctuations. A total of 2898 solar wind episodes in MAVEN and 870 solar wind episodes in Tianwen-1 are obtained. Then we choose Fourier transform to acquire power spectral densities (PSDs) for the magnetic field fluctuations.

### 2.2. Method

Figures 2(a) and (c) present two episodes of magnetic field from Tianwen-1 and MAVEN, respectively, as examples. Figures 2(b) and (d) show the corresponding PSDs as blue lines. The black lines are the smoothed PSDs using a moving window where the end frequency is 10 times higher than the starting frequency. We apply the changepoint detection

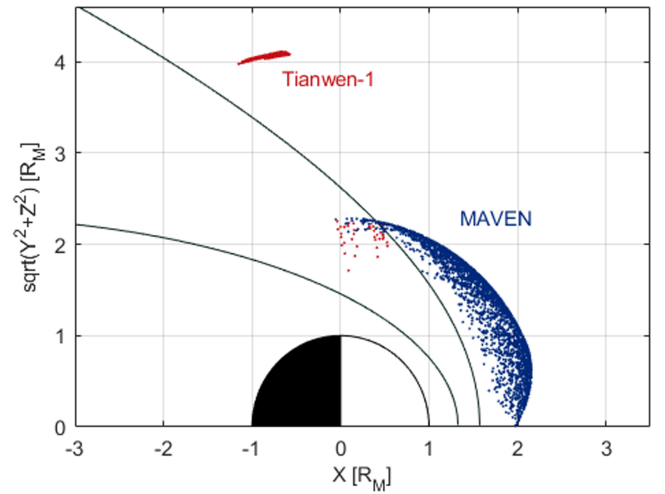


**Figure 1.** The positions of MAVEN (blue) and Tianwen-1 (red) in the Mars-centered Solar Orbital (MSO) coordinate system during 2021 November 15–December 31.

method (R. Killick et al. 2012) to the smoothed PSD to acquire the break points. We define a useful PSD as having at most four break points and each region delimited by the break points is linear. Dynamic programming methods are used to minimize the residual sum of squares of piecewise linear regression. Our results are similar to the results of L. D. Woodham et al.'s (2018) work, confirming the reliability of the method. The break points, when present, divide a PSD profile into different regions. We fit linearly to the PSD profiles within each region (red lines) to derive the spectral indices. The vertical purple line indicates the proton gyrofrequency in the spacecraft frame.

The high-frequency tails of PSDs often have a softer spectral index as shown in Figure 2. Although the PSD of the tail segment is higher than the instrument noise as indicated by the lower black line in Figure 2(b), it is probably not physical. The main reason is the aliasing effect (C. T. Russell 1972; C. Koen 2006), which means that the energy with the frequency higher than the Nyquist frequency is folded to the lower frequencies, causing the flatten phenomenon in a PSD (C. T. Russell 1972). It occurs when real signals have the component with the frequency higher than the Nyquist frequency. Our study uses the 32 Hz data from Tianwen-1 and MAVEN, corresponding to the Nyquist frequency of 16 Hz. In space, waves with frequency higher than 16 Hz should be ubiquitous, and therefore the tail in a PSD is likely to be flattened by the effect. Thus, if the spectral index of the last segment is higher than that of the previous one, the last segment is regarded as a nonphysical phenomenon and removed.

Besides, some PSDs may have prominent peaks like that around 0.9 Hz shown in Figure 2(d). Such isolated peaks possibly reflect the presence of waves or are just due to noise caused by, e.g., spacecraft maneuvers. It is difficult to distinguish the two sources in our large-sample statistical study. Thus, we simply remove all such events to make sure that our results reflect the properties of turbulence. Dozens of events are also removed manually whose fluctuations have very different properties such as Figures 2(a)–(b). The treatments result in a total of 561 Tianwen-1 events and 1685 of MAVEN events in the following analysis.

To distinguish the spectral ranges, we plot the spectral index distributions in Figure 3. We count the spectral indices of the

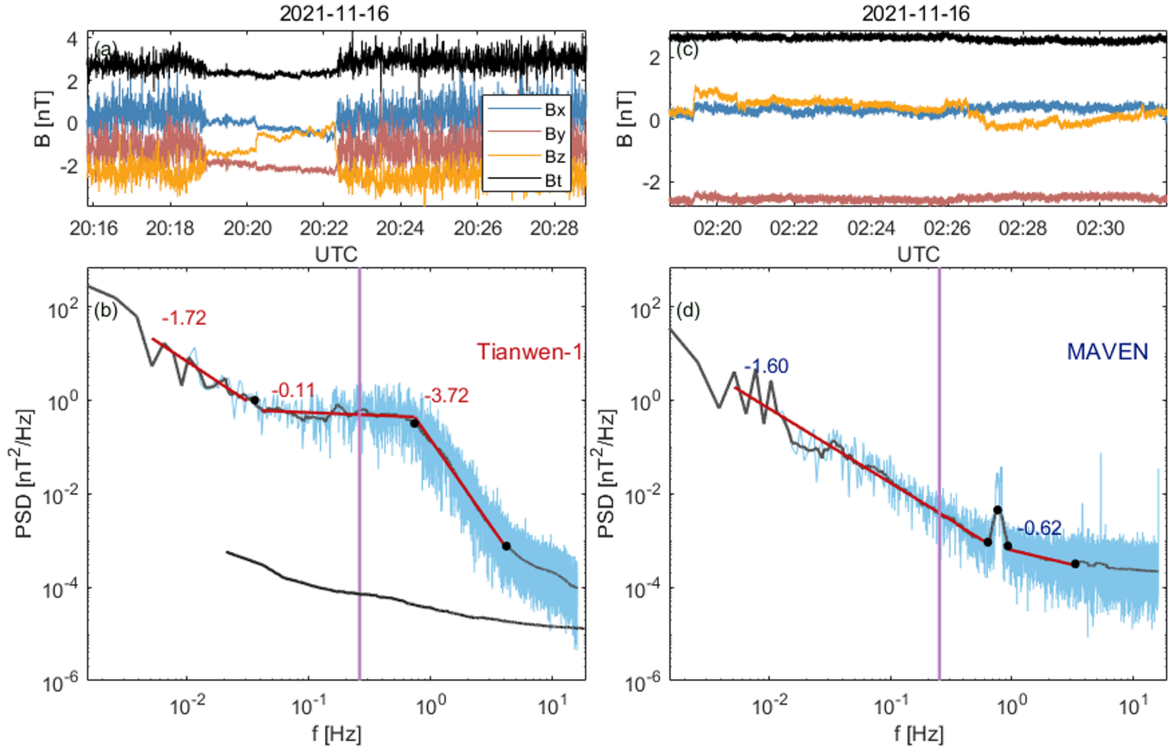


**Figure 2.** (a) An example of the analyzed magnetic field strength and x, y, z components in MSO coordinate system from Tianwen-1/MOMAG. (b) The corresponding PSDs. The blue, gray, and red lines are the original PSDs, smoothed PSDs and the piecewise fitting PSDs. The solid black dots mark the break frequencies, the numbers are the spectral indices and the purple line indicates the proton gyrofrequency. The lower black line shows the instrument noise obtained from the ground experiment. (c)–(d) An example of polluted events with the same format but from MAVEN/MAG.

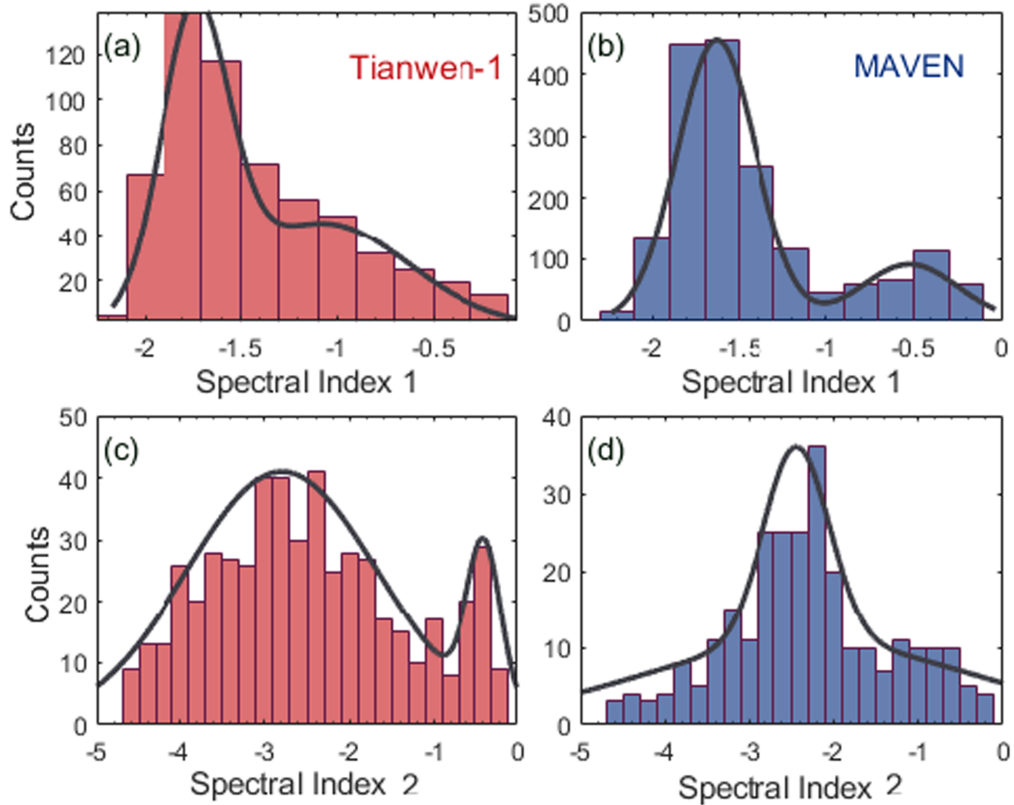


**Figure 3.** Histograms and double Gaussian distribution fitting of the low-frequency and high-frequency spectral indices. (a) The statistics of the low-frequency spectral indices in Tianwen-1. (b) The statistics of the low-frequency spectral indices in MAVEN. (c) The statistics of the high-frequency spectral indices in Tianwen-1. (d) The statistics of the high-frequency spectral indices in MAVEN.

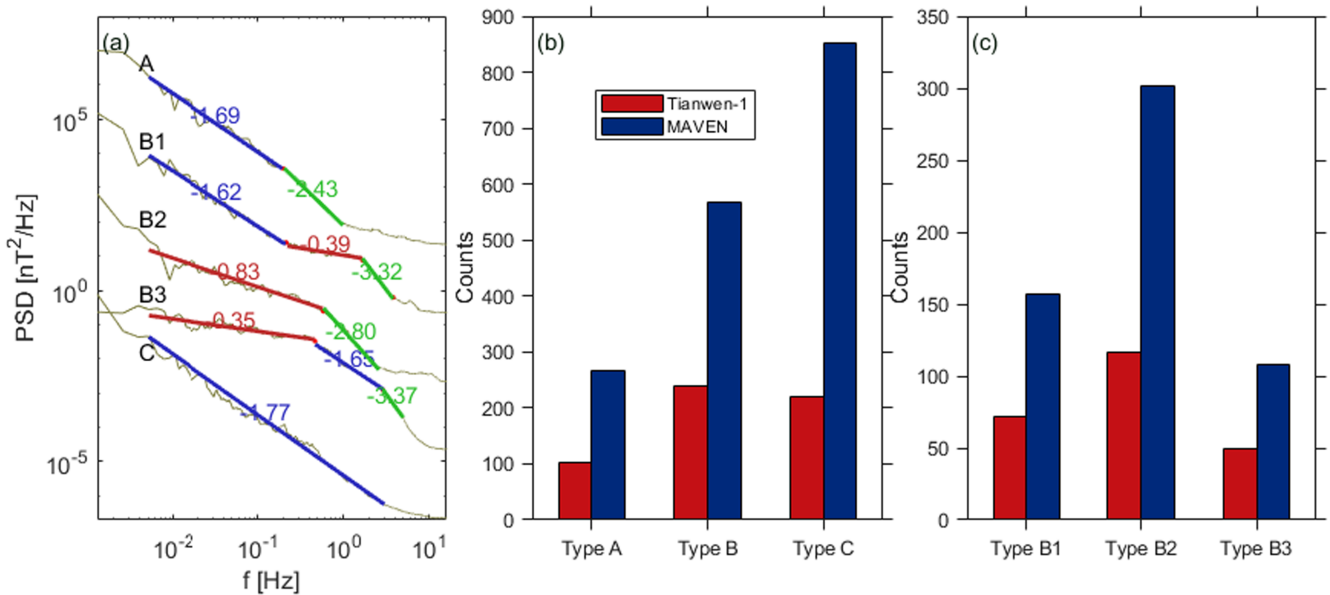


**Figure 4.** (a) Types of PSDs of magnetic field fluctuations in the Martian solar wind. The colored lines indicate fitted power-law spectra. The blue, red, and green lines represent gain range, inertial range, and dissipation range, respectively. The fitted inertial range indices and fitted dissipation range indices are shown in the legend. (b) Type A, B, and C event amounts of Tianwen-1 (red) and MAVEN (blue). (c) Type B1, B2, and B3 event amounts.

left and right segments, separated by the first break point, and fit their distributions using a double Gaussian function. In Figures 3(a)–(b), we can see that the indices of the left segments exhibit a main peak plus a minor peak. The main peak lies between  $-1.9$  and  $-1.5$ , corresponding to the inertial range because it is close to the Kolmogorov index. The minor peak has higher indices around  $-1$  for Tianwen-1 or  $-0.5$  for MAVEN, indicating deviations from the inertial range but similarities to the energy-containing range. Typically, the energy-containing range in the solar wind is below  $10^{-3}$  Hz, but here the PSDs exceed  $10^{-3}$  Hz. Thus, we define the high-index spectra as the “gain range” to differentiate them from the energy-containing range. The term “gain range” is further discussed in the last section.

Figures 3(c)–(d) show the histograms of the right segments. They also have a main peak located between  $-3$  and  $-2$ , similar to the typical spectral index of the dissipation range ( $-2.8$ ) at 1 au, and indicating the dissipation range. Meanwhile, a secondary peak appears around  $-0.4$  for Tianwen-1 and  $-1$  for MAVEN. Because the transition-range slopes at ion scales are lower than those in the inertial range (K. H. Kiyani et al. 2015; S. Y. Huang et al. 2021), the right segments have similar spectra indices to the gain range. So, in our work, they are both categorized under the “gain range.” It is interesting that the left-segment gain-range indices are larger in MAVEN than in Tianwen-1, but this trend reverses for the right segments.

According to the above statistics, we assign thresholds for range identification: inertial range ( $-1.7 \pm 0.5$ ), dissipation range ( $-2.8 \pm 0.8$ ), and gain range ( $-0.6 \pm 0.6$ ). These values and the uncertainties result from the compromise between the Gaussian fits and the boundaries between the different ranges, and ambiguous cases exist.

### 3. Classifications of Martian Turbulence Spectra

In our sample, the three ranges neither always appear nor follow a fixed order in a PSD. According to the appearance

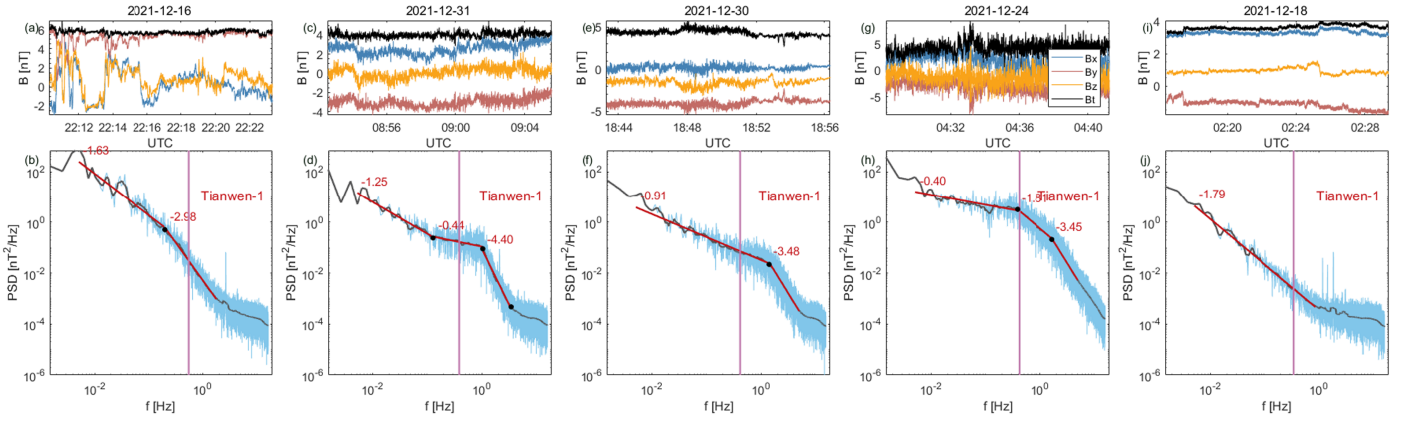
pattern of the three ranges, we divide the PSDs into three types, as shown in Figure 4. Type A is the most classic pattern, frequently observed in the solar wind at 1 au, which consists of an inertial range followed by a dissipation range. Type B has a gain range meaning energy injection, and Type C has only an inertial range. Type B can be subdivided into three spectra subtypes: B1, B2, and B3. For Type B1, the gain range appears between the inertial and dissipation ranges. For Type B2, there is no inertial range but only the gain range followed by a dissipation range. This pattern may be due to the wave energy injection replacing the inertial range by the gain range, or just simply because we do not see the inertial range being beyond the low-frequency limit of our PSDs. For Type B3, the gain range appears at the frequencies lower than the inertial range.

The examples of Types A, B1, B2, B3, and C are shown in Figure 5. These three types exhibit distinct characteristics in the magnetic field profiles. For most events, the total magnetic field remains roughly unchanged in the 13 minute time window. However, the magnetic field components of Type A and C events have different behaviors. The former usually undergoes significant variations, but the latter does not, suggesting a prominent Alfvénic characteristic for Type A events, same as the solar wind fluctuations in MHD scales (C. S. Salem et al. 2012). Compared to Types A and C, Type B events exhibit strong fluctuations in all three components, leading to the gain range appearing in the PSDs. Figure 4(b) presents the occurrence rate of Type A, B, and C events detected by Tianwen-1 and MAVEN. Only less than a quarter of the events belong to Type A. More than one-third of the events belong to Type C. The occurrence rate of the B subtypes is shown in Figure 4(c). Types B1 and B2, whose gain range connects the dissipation range, comprise the majority of Type B events.

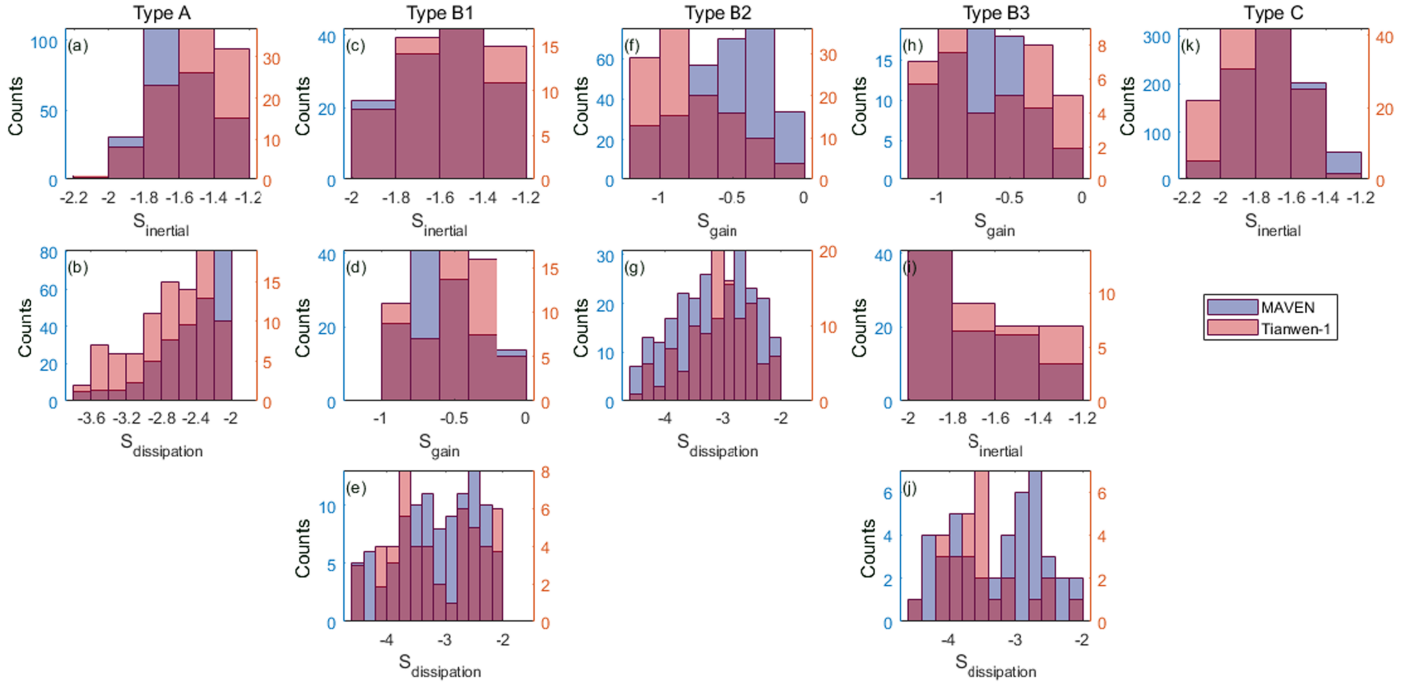
### 4. Statistical Properties of Spectral Indices

Figure 6 provides the statistical results on the spectral indices for the different types of turbulence. Figure 6(a)





**Figure 5.** Examples of the magnetic field and PSDs of Types A (a)–(b), B1 (c)–(d), B2 (e)–(f), B3 (g)–(h), and C (i)–(j) with the same formats as Figure 2.



**Figure 6.** Statistics on the spectral indices of Tianwen-1 (red) and MAVEN (blue). (a)–(b) The Type-A spectral indices of the inertial range (a) and the dissipation range (b). (c)–(e) The Type-B1 spectral indices of the inertial range (c), gain range (d), and dissipation range (e). (f)–(g) The Type-B2 spectral indices of the gain range (f) and dissipation range (g). (h)–(j) The Type-B3 spectral indices of the gain range (h), inertial range (i), and dissipation range (j). (k) The Type-C spectral indices of the inertial range.

displays the distribution of the Type-A inertial range spectral indices ( $S_i$ ) for Tianwen-1 (red) and MAVEN (blue). Their distributions are similar, with peaks around  $-1.5$  for  $S_{i,Tw}$  and around  $-1.7$  for  $S_{i,Mvn}$ , one close to the Iroshnikov–Kraichnan slope ( $-3/2$ ) and another close to the Kolmogorov slope ( $-5/3$ ). The Type-A dissipation range spectral indices ( $S_d$ ) are shown in Figure 6(b), falling between  $-3.7$  and  $-2$ , with peaks around  $-2.3$  for  $S_{d,Tw}$  and around  $-2.1$  for  $S_{d,Mvn}$ , slightly harder than those in the solar wind at 1 au.

Figures 6(c)–(j) exhibit the spectral index distribution of Types B1, B2, and B3. The inertial ranges appear only in Types B1 and B3, where the spectral index distributions from Tianwen-1 and MAVEN are highly similar. The distribution of Type-B1  $S_i$ , shown in Figure 6(d), is consistent with that of Type A, with a peak at  $\sim -1.5$ , but the spectrum of the inertial range seems to be softer in Type-B3 events with the peak at  $\sim -1.9$ .

For the dissipation range, the distributions look similar between Tianwen-1 and MAVEN (see Figures 6(e) and (g)), but different between Types B1 and B2. For Type-B1 events, it shows a bimodal distribution with peaks at around  $-2.5$  and  $-3.5$ , while for Type B2, it is a Gaussian-like distribution peaking around  $-3$ . The distributions of the dissipation range spectral indices of Type-B3 events differ between Tianwen-1 and MAVEN. The spectrum from Tianwen-1 is generally harder than those from MAVEN for the dissipation range of Type-B3 events.

The distributions of the spectral indices of gain ranges ( $S_g$ ) observed by Tianwen-1 and MAVEN are different as shown in Figures 6(d), (f), and (h). For Type B1, the spectrum from Tianwen-1 is softer than that from MAVEN (the peak of  $S_{g,Tw} \sim -0.5$  versus  $S_{g,Mvn} \sim -0.7$ ). For Type B2, the situation is reversed (the peak of  $S_{g,Tw} \sim -0.9$  versus  $S_{g,Mvn} \sim -0.3$ ). For Type B3,  $S_g$  from Tianwen-1 shows the bimodal

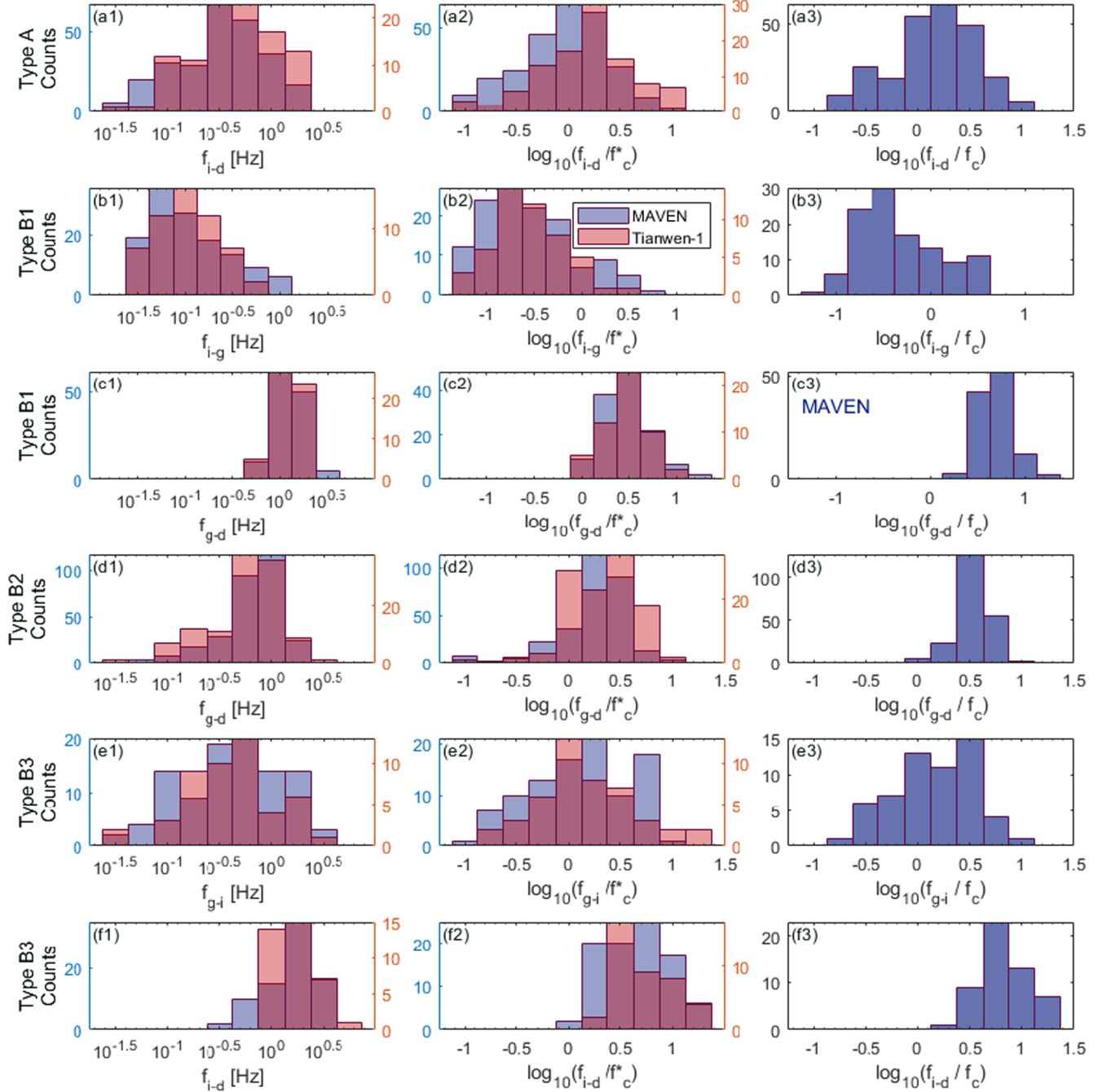


**Figure 7.** Statistics on the break frequencies of Tianwen-1 (red) and MAVEN (blue). (a1) The Type-A break frequencies between the inertial range and the dissipation range. (a2) The break frequencies shown in a1 normalized by the correctional cyclotron resonant frequencies. (a3) The Type-A break frequencies normalized by the actual cyclotron resonant frequencies in MAVEN. (b1)–(b3) The Type-B1 break-point frequencies between the inertial range and the gain range in the same form as (a1)–(a3). (c1)–(c3) The Type-B1 break-point frequencies between the gain range and the dissipation range. (d1)–(d3) The Type-B2 break-point frequencies between the gain range and the dissipation range. (e1)–(e3) The Type-B3 break-point frequencies between the gain range and the inertial range. (f1)–(f3) The Type-B3 break-point frequencies between the inertial range and the dissipation range.

distribution with the peak at around  $-0.3$  and  $-1$ , compared with the single-peak distribution from MAVEN.

Type-C events have only the inertial range. Their spectral indices are generally lower than those of Type A, and the spectra from Tianwen-1 are slightly harder than those from MAVEN, as shown in Figure 6(k). The differences in the spectral index among different types of events and between Tianwen-1 and MAVEN presented above suggest a complicated space environment surrounding Mars probably due to the presence of the bow shock and the resultant foreshock regions.

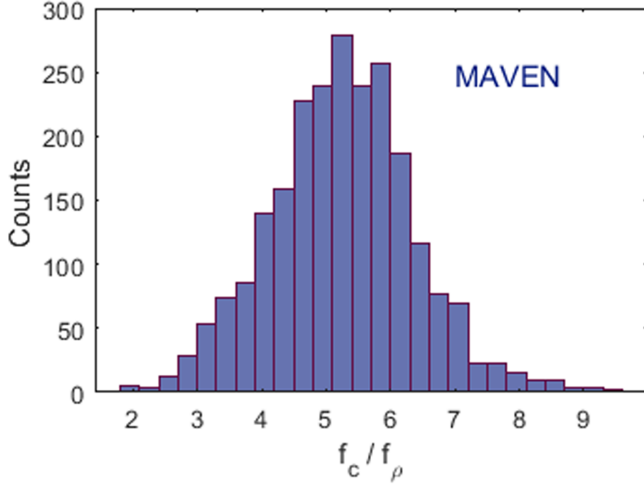
## 5. Statistical Properties of Break Frequencies

Figure 7 shows the statistics on the break frequencies between the different frequency ranges for different types of events. The first two columns exhibit the distributions of break frequencies, and the break frequencies normalized by the approximate proton cyclotron resonant frequency  $f_c^*$ , which is five times the proton gyrofrequency  $f_p$ .

According to the previous studies about the turbulence at 1 au (R. J. Leamon et al. 1998; R. Bruno & L. Trenchi 2014), the

**Table 1**  
Summary of the Peaks of the Spectral Indices and Break Frequencies (Tianwen-1 MAVEN), Some of Which Have Two Peaks

	Type A	Type B1	Type B2	Type B3	Type C
$S_i$	-1.5   -1.7	-1.5   -1.5	...	-1.9   -1.9	-1.8   -1.7
$S_d$	-2.3   -2.1	-2.7, -3.7   -2.5, -3.3	-3.1   -2.7	-3.5   -2.7	...
$S_g$	...	-0.3   -0.7	-0.9   -0.3	-0.3, -0.9   -0.7	...
$f_{i-d}/f_c^*$	1.8   1.0	...	...	3.2   5.6	...
$f_{i-g}/f_c^*$	...	0.2   0.2	...	...	...
$f_{g-i}/f_c^*$	...	...	...	1.0   1.8	...
$f_{g-d}/f_c^*$	...	3.2   3.2	3.2   1.8	...	...



**Figure 8.** Statistics on the Ratio of The Cyclotron Resonant Frequency In The Spacecraft coordinates ( $f_c$ ) to the proton gyrofrequency in plasma coordinates ( $f_\rho$ ) in MAVEN.

proton cyclotron resonant frequency  $f_c$  may differ from the local proton gyrofrequency  $f_\rho = \frac{qB}{2\pi m_p}$ , which can be directly calculated based on the magnetic field measurements from the spacecraft. C. H. K. Chen et al. (2014) pointed out that the ion cyclotron resonant scale always occurs at the larger one of the proton gyroradius  $\rho_i$  and proton inertial length  $d_i$ , and adopted  $k_c = (d_i + \rho_i)^{-1} = \Omega_i / (v_A + v_{th,i})$  to approximate the cyclotron resonant scale. Following the Taylor hypothesis, the cyclotron resonant frequency  $f_c$  can be calculated as  $f_c = \frac{k_c \cdot V_{sw}}{2\pi}$ . For MAVEN, we can obtain  $f_c$  according to the SWIA and MAG data. However, we cannot obtain  $f_c$  for Tianwen-1 due to the lack of the complete plasma data. To solve this problem, we compare the values of  $f_c$  and  $f_\rho$  using MAVEN data and find that the distribution of their ratio is around 5, as shown in Figure 8. Thus, we define the approximated proton cyclotron resonant frequency  $f_c^*$  as  $5f_\rho$ , and use it to normalize the observed break frequencies in Figure 7.

Back to Figure 7, we can find that the distributions of the break frequencies from Tianwen-1 and MAVEN are similar though small differences exist. The break frequency between the inertial range and dissipation range ( $f_{i-d}$ ), which is only available for Type-A and Type-B3 events, is generally larger than the cyclotron resonant frequency, and the break frequency in Type-B3 events, around 1.8 Hz or  $4.2 f_c^*$ , is larger than 0.3 Hz or  $1.3 f_c^*$  in Type A (Figures 7(a1), (a2), (f1), and (f2)).

This illustrates that  $f_c^*$  is still a characteristic frequency of turbulence dissipation in Type-A events.

The other break frequencies shown in Figure 7 are between the gain range and other types of ranges. The Type-B1 events have the break frequencies  $f_{i-g}$  between the inertial range and the gain range, which vary widely from 0.03 to 1 Hz with the peak of the distribution at around  $0.2 f_c^*$  (Figures 7(b1) and (b2)). The reversed situation happens in Type-B3 events, in which the gain range appears at the low-frequency end of the inertial range leading to the break frequency of  $f_{g-i}$ . Compared to the distribution of  $f_{i-g}$ , the distribution of  $f_{g-i}$  roughly shifts toward high frequency by an amount of about 0.75 in logarithmic scale with the peak at around  $1.3 f_c^*$  (Figures 7(e1) and (e2)). The break frequencies between the gain range and the dissipation range ( $f_{g-d}$ ) appear in Type-B1 and -B2 events. The distributions for the two types of events are similar with the peaks around 1 Hz or  $3.2 f_c^*$ . The distribution for Type B1, ranging between 0.2 and 4.2 Hz (or 1 and  $10 f_c^*$ ), is more concentrated than that for Type B2.

To validate the usage of  $f_c^*$ , the last column shows the distributions of the break frequencies normalized by the proton cyclotron resonant frequencies  $f_c$  for MAVEN data. The distributions are similar to the MAVEN's distributions in the second column though small differences exist, proving the validity of  $f_c^*$  in this analysis.

## 6. Summary and Discussion

In our work, we acquired the Martian solar wind turbulence spectra of the 46 day data set observed by Tianwen-1 and MAVEN simultaneously and divide them into Type A to Type C. Table 1 summarizes the spectral indices and break frequencies derived from our analysis. Only fewer than a quarter of the events have and only have inertial range and dissipation range, which are classified as Type A. The turbulence is fully developed in Type A, with the energy cascading in the inertial range and dissipating in some ion-scale dissipation mechanisms, such as cyclotron damping (C. H. K. Chen et al. 2014). Their  $S_i$  and  $S_d$  have the same characteristics as the 1 au PSDs. The  $f_{i-d}$  is the same and close to the cyclotron resonant frequency.

The appearance of the gain range forms the Type-B spectra, which indicate the energy injection in some scales. The Type-B  $S_d$  is lower than the Type-A  $S_d$  and the Type-B3  $S_i$  is lower than the other  $S_i$  remarkably. This suggests that the gain range appearance is accompanied by the faster energy dissipation in the higher frequencies, which means the more frequent fluctuations in kinetic scales such as whistlers or kinetic Alfvén waves. Meanwhile, the appearance of the gain range

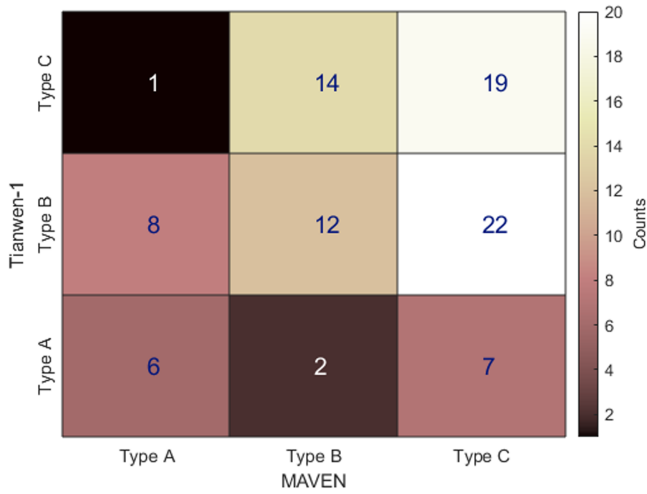


**Figure 9.** Statistics on the types of the events observed by the two satellites simultaneously.

also causes the break frequency,  $f_{g-d}$  or  $f_{i-d}$ , of the dissipation range shifting to the higher frequency.

In Martian solar wind, the energy injection of Type-B spectra may be associated with some fluctuations or some structures. Here we try to explain the possible sources of their energy injection. The shape of the Type-B1 spectra is the same as the plateau-like spectra (W. Jiang et al. 2023; H. Li et al. 2024), and the pickup ions could be accelerated and form the “1 Hz” wave (Z. Su et al. 2023). The Type-B2 spectra are often seen in the magnetosheath, and in the Martian solar wind, the superposition of fluctuations and the inverse cascades of energy could form the Type-B2 spectra, similar to the spectra indices in the energy-containing range (R. Marino & L. Sorriso-Valvo 2023). The Type-B3 spectra could be due to lower frequency waves such as 30 s waves (Z. Su et al. 2023) or the structures caused by magnetic field swerving in the foreshock (G. Collinson et al. 2017; H. Madanian et al. 2023). The cause of the Type-B spectra needs to be further investigated in case studies, and the injection of energy and the inverse cascading process deserve further study.

It should be noted that we use the term “gain range” rather than the transition range (K. H. Kiyani et al. 2015; S. Y. Huang et al. 2021) or the energy-containing range. Our consideration is based on both the spectral index and the break frequencies. Take Type B1 as an example, the break frequency between the gain range and the inertial range,  $f_{i-g}$ , is generally lower than the ion cyclotron resonant frequency,  $f_c^*$  (Figure 7(b)), whereas the break frequency between the gain range and the dissipation range,  $f_{g-d}$ , is generally higher than  $f_c^*$  (Figure 7(c)). Thus, the gain range spans over the ion characteristic frequency, crossing the MHD range and kinetic range. Compared to the transition range, the gain range defined here is different. (1) The transition ranges mostly appear in the kinetic range. The gain ranges in Type B1 do not. (2) The transition ranges mostly have a spectral index less than that of the inertial range and even less than that of the dissipation range. The gain ranges in Type B1 are not. On the other hand, the spectral index of the gain range is not always close to that of the energy-containing range, sometimes the gain range has a higher spectral index. Meanwhile, the energy-containing range usually appears at a frequency lower than 0.001 Hz, much lower than the frequencies investigated in our study. That is why we prefer to call it “gain” range, suggesting

that some energy is gained neither like the transition range nor the energy-containing range. The reason for the gain range of Types B2 and B3 is similar.

The Type-C spectra appear in more than a third of the PSDs, without a dissipation range. The Type-C  $S_i$  are lower than those of Type A overall. The missing dissipation range is probably due to it shifts to a higher frequency, which is contaminated by the flattened tail (Figure 2). This could be due to the lower ion density and the lower magnetic field of the Martian solar wind, compared with the solar wind at 1 au.

Different from the PSDs in 1 au, the flattened tail is more frequently observed in Martian solar wind. Besides the reason of the aliasing effect mentioned before, another plausible explanation for these flattened spectral tails could be the breakdown of the Taylor hypothesis (K. G. Klein et al. 2014). Specifically, the whistler turbulence could violate the Taylor hypothesis. If the explanation holds true, the Martian solar wind turbulence may be whistler rather than Alfvénic in kinetic scale, which needs to be verified by further work.

Our analysis reveals that the spectra from Tianwen-1 are more or less different from those from MAVEN. A probable reason is that Tianwen-1 and MAVEN collected the data at different regions though they are both in solar wind (see Figure 1). To clearly see the difference of the spectra from the two spacecraft, we examine all 91 episodes during which both Tianwen-1 and MAVEN were in solar wind at the same time. As revealed by Figure 9, it is found that in 40.7% of the episodes the spectra from the two spacecraft are classified into the same types. This means that the two spacecraft observed different types of events in 59.3% of the episodes, suggesting a notable variation upstream of the Martian bow shock. Concretely, more than half of the Type-A events at MAVEN happen with the occurrence of Type-B events at Tianwen-1, more than half of the Type-B events at MAVEN with Type-C events at Tianwen-1, and more than half of the Type-C events at MAVEN with Type-B (some to Type-A) events at Tianwen-1. These changes lead to 50% more Type-B events being observed by Tianwen-1 than by MAVEN. The cause of such changes should be related to local characteristics, e.g., the presence of the foreshock. We may speculate that the energy injection more frequently happens at the flank of the bow shock than at the nose. More detailed analysis in the future is required to reveal the causes of the discrepant spectra between the two spacecraft.

### Acknowledgments







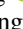





This work in China was supported by the NSFC (grant Nos. 42130204, 42188101, 42241155, and 42404164) and the Strategic Priority Program of the Chinese Academy of Sciences (grant No. XDB41000000). Y.W. is particularly grateful to the support of the Tencent Foundation.

### Data Availability

The MAVEN spacecraft data used in this study are publicly available through the Planetary Data System: J. E. P. Connerney (2017) for MAG and J. S. Halekas (2017) for SWIA. The Tianwen-1/MOMAG data are publicly available at CNSA Data Release System (<http://202.106.152.98:8081/marsdata/>) or the official website of the MOMAG team ([http://space.ustc.edu.cn/dreams/tw1\\_momag/](http://space.ustc.edu.cn/dreams/tw1_momag/)).



## ORCID iDs

Zhuxuan Zou  <https://orcid.org/0009-0008-9920-9600>  
 Yuming Wang  <https://orcid.org/0000-0002-8887-3919>  
 Zhenpeng Su  <https://orcid.org/0000-0001-5577-4538>  
 Long Cheng  <https://orcid.org/0000-0003-0578-6244>  
 Zhiyong Wu  <https://orcid.org/0000-0002-1169-3493>  
 Tielong Zhang  <https://orcid.org/0000-0002-0980-6292>  
 Guoqiang Wang  <https://orcid.org/0000-0002-6618-4928>  
 Yutian Chi  <https://orcid.org/0000-0001-9315-4487>  
 Zonghao Pan  <https://orcid.org/0000-0003-2626-4824>  
 Xinjun Hao  <https://orcid.org/0009-0008-2433-0465>  
 Yiren Li  <https://orcid.org/0009-0000-3310-519X>  
 Kai Liu  <https://orcid.org/0000-0003-2573-1531>

## References

- Alexandrova, O., Carbone, V., Veltri, P., & Sorriso-Valvo, L. 2008, *ApJ*, **674**, 1153
- Alexandrova, O., Chen, C. H. K., Sorriso-Valvo, L., Horbury, T. S., & Bale, S. D. 2013, *SSRv*, **178**, 101
- Alexandrova, O., Lacombe, C., Mangeney, A., Grappin, R., & Maksimovic, M. 2012, *ApJ*, **760**, 121
- Alexandrova, O., Saur, J., Lacombe, C., et al. 2009, *PhRvL*, **103**, 165003
- Anderson, B. J., Acuña, M. H., & Lohr, D. A. 2007, *SSRv*, **131**, 417
- Balogh, A., Beek, T. J., Forsyth, R. J., et al. 1992, *A&AS*, **92**, 221
- Borovsky, J. E. 2012, *JGRA*, **117**, A05104
- Bruno, R., & Trenchi, L. 2014, *ApJL*, **787**, L24
- Bruno, R., Trenchi, L., & Telloni, D. 2014, *ApJL*, **793**, L15
- Carbone, V. 2012, *SSRv*, **172**, 343
- Chen, C. H. K., Bale, S. D., Bonnell, J. W., et al. 2020, *ApJS*, **246**, 53
- Chen, C. H. K., Leung, L., Boldyrev, S., Maruca, B. A., & Bale, S. D. 2014, *GRL*, **41**, 8081
- Collinson, G., Sibeck, D., Omid, N., et al. 2017, *JGRA*, **122**, 9910
- Connerney, J. E. P. 2017, NASA Planetary Data System, urn:nasa:pds:maven.mag.calibrated:data.ss::2.3, doi:10.17189/1414251
- Connerney, J. E. P., Espley, J., Lawton, P., et al. 2015, *SSRv*, **195**, 257
- Davis, N., Chandran, B. D. G., Bowen, T. A., et al. 2023, *ApJ*, **950**, 154
- Delva, M., Mazelle, C., Bertucci, C., et al. 2011, *SSRv*, **162**, 5
- Dorseth, M., Perez, J. C., Bourouaine, S., Palacios, J. C., & Raouafi, N. E. 2024, *A&A*, **689**, A117
- Duan, D., Bowen, T. A., Chen, C. H. K., et al. 2020, *ApJS*, **246**, 55
- Halekas, J. S. 2017, NASA Planetary Data System, urn:nasa:pds:maven.swia.calibrated:data.onboard\_svy\_mom::1.11, doi:10.17189/1414246
- Halekas, J. S., Taylor, E. R., Dalton, G., et al. 2015, *SSRv*, **195**, 125
- Huang, S. Y., Sahraoui, F., Andrés, N., et al. 2021, *ApJL*, **909**, L7
- Jannet, G., Dudok, W., Krasnoselskikh, V., et al. 2021, *JGRA*, **126**, e28543
- Jiang, W., Li, H., Liu, X., Verscharen, D., & Wang, C. 2023, *JGRA*, **128**, e2022JA030874
- Killick, R., Fearnhead, P., & Eckley, I. A. 2012, *JASA*, **107**, 1590
- Kiyani, K. H., Osman, K. T., & Chapman, S. C. 2015, *RSPTA*, **373**, 2041
- Klein, K. G., Howes, G. G., & TenBarge, J. M. 2014, *ApJL*, **790**, L20
- Koen, C. 2006, *MNRAS*, **371**, 1390
- Leamon, R. J., Smith, C. W., Ness, N. F., Matthaeus, W. H., & Wong, H. K. 1998, *JGR*, **103**, 4775
- Li, H., Jiang, W., Yang, Z., et al. 2024, *ApJ*, **967**, 76
- Liu, K., Hao, X., Li, Y., et al. 2020, *E&PP*, **4**, 384
- Lotz, S., Nel, A. E., Wicks, R. T., et al. 2023, *ApJ*, **942**, 93
- Madanian, H., Omid, N., Sibeck, D. G., et al. 2023, *GRL*, **50**, e2022GL101734
- Marino, R., & Sorriso-Valvo, L. 2023, *PhR*, **1006**, 1
- Markovskii, S. A., Vasquez, B. J., & Smith, C. W. 2008, *ApJ*, **675**, 1576
- Matthaeus, W. H., & Goldstein, M. L. 1986, *PhRvL*, **57**, 495
- Mazelle, C., Winterhalter, D., Sauer, K., et al. 2004, *SSRv*, **111**, 115
- Narita, Y. 2016, *ApJ*, **831**, 83
- Podesta, J. J., Roberts, D. A., & Goldstein, M. L. 2007, *ApJ*, **664**, 543
- Ruhunusiri, S., Halekas, J. S., Espley, J. R., et al. 2017, *JGRA*, **122**, 656
- Russell, C. T. 1972, *NASSP*, **308**, 365
- Salem, C. S., Howes, G. G., Sundkvist, D., et al. 2012, *ApJ*, **745**, L9
- Smith, C. W., Vasquez, B. J., & Hollweg, J. V. 2012, *ApJ*, **745**, 8
- Su, Z., Wang, Y., Zhang, T., et al. 2023, *ApJL*, **947**, L33
- Wang, Y., Zhang, T., Wang, G., et al. 2023, *E&PP*, **7**, 216
- Woodham, L. D., Wicks, R. T., Verscharen, D., & Owen, C. J. 2018, *ApJ*, **856**, 49
- Zimbardo, G., Greco, A., Sorriso-Valvo, L., et al. 2010, *SSRv*, **156**, 89
- Zou, Z., Wang, Y., Zhang, T., et al. 2023, *ScChE*, **66**, 2396